Improving Li-ion interfacial transport in hybrid solid electrolytes

Liu, Ming; Zhang, Shengnan; van Eck, Ernst R.H.; Wang, Chao; Ganapathy, Swapna; Wagemaker, Marnix

Important note
To cite this publication, please use the final published version (if applicable).
Please check the document version above.

Check for updates

Improving Li-ion interfacial transport in hybrid solid electrolytes

Ming Liu[1], Shengnan Zhang[1], Ernst R. H. van Eck[2], Chao Wang[1], Swapna Ganapathy [1✉]
and Marnix Wagemaker [1✉]

The development of commercial solid-state batteries has to date been hindered by the individual limitations of inorganic and organic solid electrolytes, motivating hybrid concepts. However, the room-temperature conductivity of hybrid solid electrolytes is still insufficient to support the required battery performance. A key challenge is to assess the Li-ion transport over the inorganic and organic interfaces and relate this to surface chemistry. Here we study the interphase structure and the Li-ion transport across the interface of hybrid solid electrolytes using solid-state nuclear magnetic resonance spectroscopy. In a hybrid solid polyethylene oxide polymer–inorganic electrolyte, we introduce two representative types of ionic liquid that have different miscibilities with the polymer. The poorly miscible ionic liquid wets the polymer–inorganic interface and increases the local polarizability. This lowers the diffusional barrier, resulting in an overall room-temperature conductivity of 2.47×10^{-4} S cm^{-1}. A critical current density of 0.25 mA cm^{-2} versus a Li-metal anode shows improved stability, allowing cycling of a LiFePO$_4$–Li-metal solid-state cell at room temperature with a Coulombic efficiency of 99.9%. Tailoring the local interface environment between the inorganic and organic solid electrolyte components in hybrid solid electrolytes seems to be a viable route towards designing highly conducting hybrid solid electrolytes.

Solid-state batteries are recognized as key candidates for next generation batteries because of their potential to improve both energy density and safety[1,2]. However, the progress in their development is hindered by the many criteria that solid electrolytes must satisfy to become commercially viable. These include high ionic conductivity, flexibility, (electro)chemical stability, compatibility with electrode materials and processability, conditions that are often hard to fulfill with an individual organic or inorganic solid electrolyte material[3–7]. This has led to the investigation of hybrid electrolytes that typically combine an organic and an inorganic phase[8–11]. An intensively investigated hybrid solid electrolyte (HSE) comprises inorganic filler particles embedded in a conductive organic polymer matrix. The use of polyethylene oxide (PEO) as the organic polymer component together with a Li-containing salt is attractive because of its relative stability towards lithium metal, excellent contact/adhesion with electrodes, superior mechanical properties and good flexibility, allowing facile production as thin films on a large scale[12–17]. Properties such as particle size, relative amount and morphology of the inorganic component influence the conductivity of the HSE. Typically, inorganic fillers are added to lower the glass transition temperature of PEO. This enhances the polymer chain segmental mobility and results in higher ionic conductivity[13,18–20].

More recently, HSEs with inorganic ionic conductors as additives have been investigated with the aim to provide highly conductive pathways for Li-ion transport to improve the overall conductivity of the HSE (refs. [18,20–24]). However, despite the high ionic conductivity of these inorganic fillers (for example > 1 mS cm^{-1}), their room-temperature Li-ion conductivity remains far from what is demanded for all-solid-state-batteries (~1 mS cm^{-1}). This raises questions about the Li-ion transport pathway through the heterogeneous HSE, and especially on the role of the interface between

the organic and inorganic components. However, it is challenging to monitor the Li-ion transport in HSEs at the sub-nano scale of interfaces. Several approaches have been reported that explore the correlation between interface environment and Li-ion movement in HSEs (refs. [4,18,25–28]). Three-dimensional (3D) structural reconstruction of HSEs obtained from synchrotron experiments and physics-based modelling indicates that the inorganic particles are highly aggregated in the electrolyte, which would affect the internal Li-ion transport between different phases[4,25]. Four-point electrochemical impedance measurements and surface-sensitive X-ray photoelectron spectroscopy revealed decomposition reactions between the organic and inorganic phases, which may significantly affect the Li-ion transport[26,27]. Recently, combining selective isotope labelling with high-resolution solid-state nuclear magnetic resonance (NMR), Li-ion diffusion pathways were tracked within a Li$_7$La$_3$Zr$_2$O$_{12}$ (LLZO)–PEO HSE (refs. [18,28]). While these studies provide insight into Li-ion transport in HSEs, it is also evident that it remains a challenge to directly access the interfacial structure, correlate this to the Li-ion transport across the interface and use this to develop strategies to improve the conductivity of HSEs (ref. [10]).

To gain deeper insight into the Li-ion transport in HSEs in conjunction with the inorganic–organic interphase structure, we employed an experimental approach using electrochemical impedance spectroscopy (EIS) and multinuclear solid-state NMR. This allows us to measure the bulk conductivity as well as directly access the interphase structure and interfacial Li-ion diffusion in an HSE comprising an LiTFSI (lithium-bis (trifluoromethane-sulfonyl) imide)–PEO organic and an argyrodite Li$_6$PS$_5$Cl inorganic component. We find that the ionic conductivity of the HSE is impeded by the chemical structure of the decomposition layer between the organic and inorganic phases. To overcome this the interface is 'activated' by adding an ionic liquid that settles at the organic–inorganic
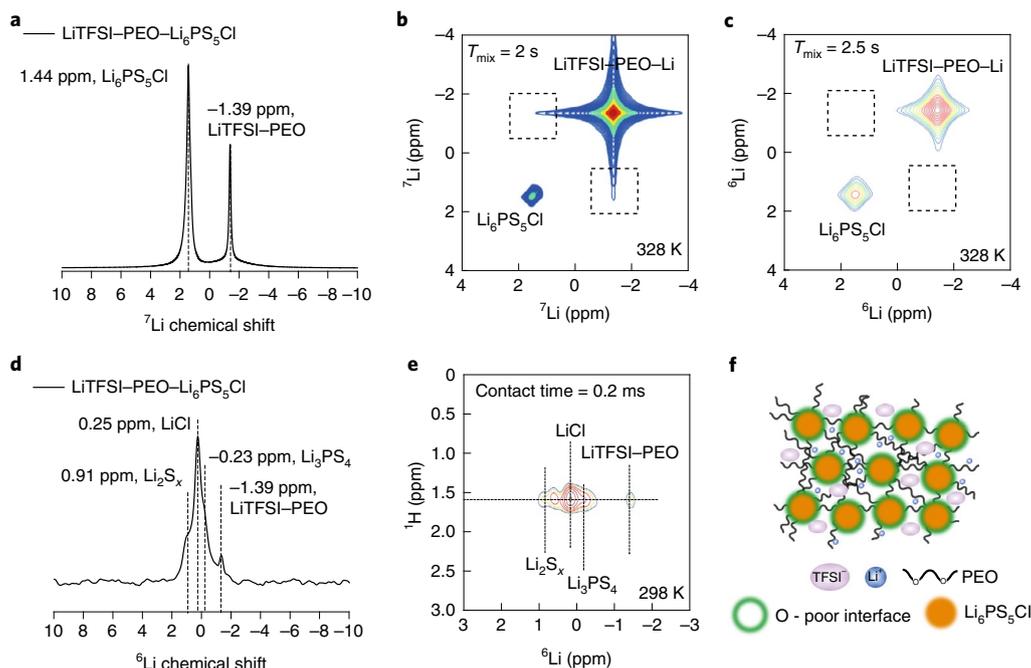
Fig. 1 | Li-ion interface diffusion between LiTFSI–PEO and Li₆PS₅Cl. a–c, 1D ^{7}Li MAS spectrum (**a**) and ^{7}Li–^{7}Li (**b**) and ^{6}Li–^{6}Li (**c**) 2D-EXSY spectra corresponding to the LiTFSI–PEO–Li₆PS₅Cl HSE with mixing times of 2 and 2.5 s at 328 K, where no obvious off-diagonal cross-peak intensity is observed, indicating that the exchange flux of Li ions over the solid–solid LiTFSI–PEO–Li₆PS₅Cl interface is very small. **d**, 1D ^{1}H–^{6}Li CPMAS spectrum with a contact time of 6 ms (200 μs–6 ms can be found in Extended Data Fig. 2), measured at a spinning speed of 5 kHz. One thousand and twenty-four scans were acquired with a recycle delay of 20 s. **e**, A 2D ^{1}H–^{6}Li HETCOR spectrum measured with a CP contact time of 0.2 ms. **f**, Schematic figure of Li-ion diffusion pathway in the HSE. Intensity from low to high is depicted as blue to red in **b**, **c** and **e**.

interface of the HSE because it is poorly miscible with PEO. This enables Li-ion diffusion over the interface, which increases the overall ionic conductivity of the HSE as visualized by two-dimensional (2D) ^{7}Li exchange NMR. Solid-state NMR is demonstrated to be a powerful method for resolving the sub-nano domains of the interface, which is impossible by other traditional characterization techniques. In this manner the bottleneck for Li-ion transport in HSEs is revealed and new design strategies are proposed towards future solid electrolytes.

Interphase structure and Li-ion diffusion in the hybrid LiTFSI–PEO–Li₆PS₅Cl solid electrolyte

With the aim of improving the overall Li-ion conductivity of a LiTFSI–PEO polymer electrolyte, highly conductive micron-sized argyrodite Li₆PS₅Cl (5.6 mS cm⁻¹) was mixed into the LiTFSI–PEO with a weight fraction of 10% (scanning electron microscope (SEM) images in Extended Data Fig. 1). For Li₆PS₅Cl to contribute to the bulk conductivity of this HSE, facile Li-ion diffusion over the interfaces between the LiTFSI–PEO phase and the Li₆PS₅Cl particles is a prerequisite. This is because a 10% weight fraction (8% volume fraction) will not result in percolating transport pathways through the Li₆PS₅Cl phase. Li₆PS₅Cl was selected as the inorganic filler to facilitate interfacial transport as it possesses both high ionic conductivity and high ductility, the latter enabling the formation of softer interfaces that facilitate interfacial Li-ion diffusion[29]. To study the Li-ion diffusion across the LiTFSI–PEO–Li₆PS₅Cl interface and to resolve the interphase structure between the organic and inorganic phases, magic angle spinning (MAS) ^{6,7}Li solid-state NMR was employed. This allows us to discriminate between Li ions in different chemical environments, in this case in the PEO and Li₆PS₅Cl phases[18,29]. As seen in Fig. 1a, the LiTFSI–PEO and Li₆PS₅Cl show two clear resonances with ^{7}Li chemical shifts of −1.39 and 1.44 ppm, respectively.

Based on the differences in ^{6,7}Li chemical shifts of the LiTFSI–PEO and Li₆PS₅Cl phases, 2D exchange spectroscopy (2D-EXSY) experiments provide selective and non-invasive quantification of the spontaneous Li-ion diffusion over the solid–solid interface between these phases[29,30]. Li-ion exchange between these two chemical environments would result in off-diagonal cross-peaks at the positions indicated with dotted boxes in Fig. 1b,c. Increasing the mixing time, T_{mix}, therefore providing more time for the Li ions to diffuse from one phase to the other, as well as increasing the temperature, is expected to increase the Li-ion exchange flux and thus the intensity of the off-diagonal cross-peaks[29]. In this case the absence of cross-peaks, even for the maximum T_{mix} and temperature (T_{mix} = 2 s and 2.5 s, 328 K) that can be achieved, indicates that the Li-ion exchange (flux) between LiTFSI–PEO and Li₆PS₅Cl phases does not occur at the timescale of T_{mix}, indicating very slow Li-ion diffusion across the interfaces within this HSE.

To discern the origin of the poor Li-ion diffusion across these interfaces, one-dimensional (1D) ^{6}Li cross-polarization (CP) MAS (CPMAS) and 2D ^{1}H–^{6}Li heteronuclear correlation (HETCOR) experiments were carried out (Fig. 1d,e), allowing us to resolve the interface composition and structure. In these experiments, transfer of polarization occurs from protons (^{1}H), in this case abundantly present in the polymer, to any ^{6}Li environment in the near vicinity (within the range of a few bonds). This takes place during a varying time interval (contact time), typically in the range 200 μs–6 ms (Extended Data Fig. 2). With direct ^{6,7}Li excitation, only two peaks are resolved as shown in Fig. 1a for ^{7}Li (Extended Data Fig. 3 for ^{6}Li). However, in the ^{6}Li CPMAS spectrum several additional resonances between 1 ppm and −1.5 ppm (Fig. 1d) are resolved. The additional peaks are assigned to Li-containing polysulfides and phosphorus sulfide species[31,32], based on previous literature[26,27]. This indicates that inorganic decomposition products that could inhibit interfacial
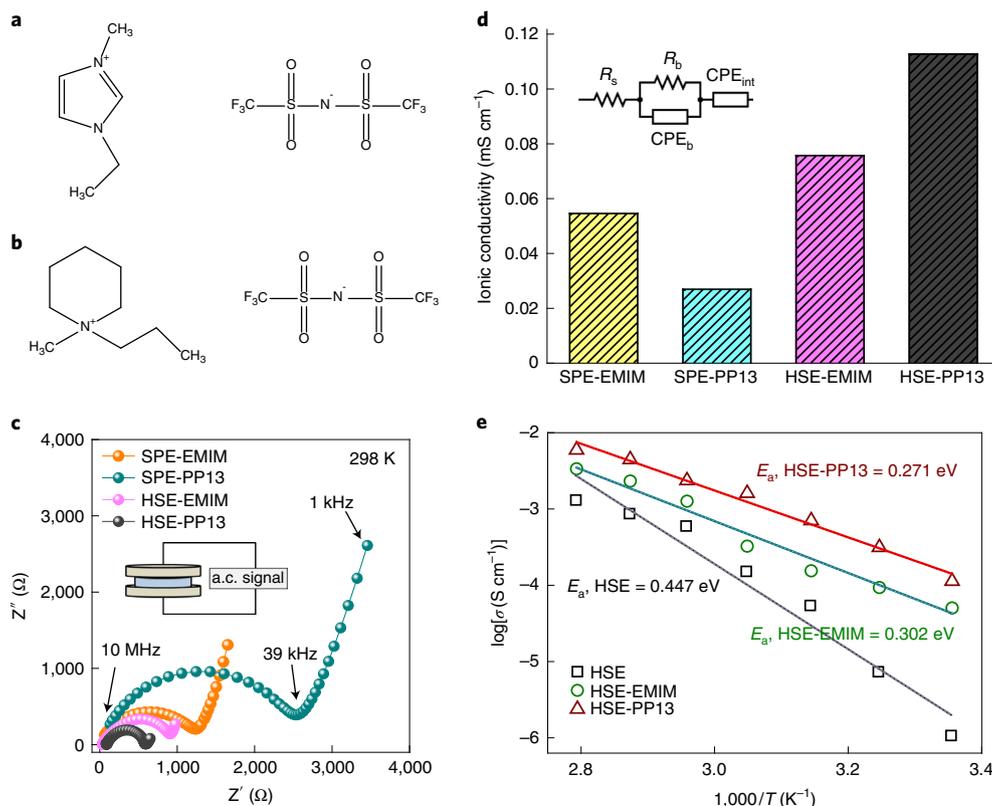
Fig. 2 | Macroscopic diffusion in HSEs with PP13-TFSI and EMIM-TFSI IL additives. a,b, Molecular structures of PP13-TFSI and EMIM-TFSI ILs. **c,d**, EIS measurements and ionic conductivity of cells with LiTFSI–PEO solid polymer electrolytes with PP13-TFSI (SPE-PP13, 2.69×10^{-5} S cm^{-1} at 25 °C) and EMIM-TFSI (SPE-EMIM, 5.45×10^{-5} S cm^{-1} at 25 °C) ILs and LiTFSI–PEO–Li$_6$PS$_5$Cl HSEs with PP13-TFSI (HSE-PP13, 1.12×10^{-4} S cm^{-1} at 25 °C) and EMIM-TFSI (HSE-EMIM, 7.57×10^{-5} S cm^{-1} at 25 °C) ILs. The contact area with the stainless steel current collector is 1.13 cm^2. **e**, Ionic conductivity determined by impedance spectroscopy measurements of LiTFSI–PEO–Li$_6$PS$_5$Cl HSE ($E_a = 0.447$ eV) and with PP13-TFSI (HSE-PP13, $E_a = 0.271$ eV) and EMIM-TFSI (HSE-EMIM, $E_a = 0.302$ eV) ILs at various temperatures. a.c., alternating current.

Li-ion transport accumulate at the interface. The 2D ^{1}H–^{6}Li experiment at a short contact time shows correlations between ^{1}H and ^{6}Li species either directly bonded to, or in very close proximity to, each other. At a short contact time of 0.2 ms (Fig. 1e, in Extended Data Fig. 2 peaks are also visible at 0.2 ms) the different Li species observed are in contact with a single ^{1}H environment at a chemical shift of ~1.6 ppm, which can be assigned to the –OCH$_2$– group. This has been identified from X-ray photoelectron spectroscopy studies[26,27,33] as the main decomposition product of PEO chains when in contact with Li$_6$PS$_5$Cl and indicates that there are interfacial reactions between Li$_6$PS$_5$Cl and PEO. These reactions result in an inert environment deficient in ethereal oxygen that is known to mediate the Li-ion diffusion in PEO (Fig. 1f). The poorly Li-ion conducting interface environment is held responsible for the absence of Li-ion exchange (Fig. 1b,c), indicating sluggish Li-ion diffusion between the two electrolyte phases. These findings can potentially explain the difficulties in activating inorganic particles in HSEs (ref. [18]), indicating that the interface needs to be improved to enhance the interfacial Li-ion diffusion.

Addition of ionic liquids to enhance the conductivity of the PEO–Li$_6$PS$_5$Cl hybrid solid electrolyte

Based on the above findings, it is clear that an inert interface is formed between LiTFSI–PEO and Li$_6$PS$_5$Cl that impedes charge transport in the HSE. Traditionally, ionic liquids (ILs) have been used to enhance the segmental motion of PEO chains to increase the Li-ion mobility[9,34]. These ILs do not form strong ionic bonds between their cation and anion moieties and hence possess low

solvation energies and remain in a dissociated state. It has been shown in previous studies that imidazole-based ILs are effective in improving the conductivity of PEO because of their low viscosity and high miscibility in PEO (ref. [34]).

To determine whether an IL added to the HSE has an impact on the conductivity and interfacial charge diffusivity between the organic and inorganic phases, two ILs that differ significantly in their viscosity and miscibility with PEO were selected. The first was an imidazole-based IL, 1-ethyl-3-methylimidazolium bis(trifluoromethylsulfonyl)imide (denoted as EMIM-TFSI) (Fig. 2a) and the second was a piperidinium-based IL, 1-methyl-1-propylpiperidinium bis(trifluoromethylsulfonyl)imide (denoted as PP13-TFSI) (Fig. 2b). These ILs each have a different miscibility in PEO (ref. [35]) where the hypothesis is that the poorly miscible PP13-TFSI will be preferably located at the interface with the inorganic Li$_6$PS$_5$Cl phase, with the aim to improve the Li-ion diffusion across the interface. By contrast, the highly miscible EMIM-TFSI is anticipated to be distributed homogenously in the HSE and to not specifically influence Li-ion transport across the organic–inorganic interface. To test this, fixed amounts of EMIM-TFSI and PP13-TFSI (0.25:1 molar ratio IL:LiTFSI) were added to the LiTFSI–PEO–Li$_6$PS$_5$Cl mixture. The HSEs subsequently formed are henceforth referred to as HSE-EMIM and HSE-PP13, respectively.

To establish how the addition of the ILs improves the macroscopic conductivity of the PEO electrolyte (no Li$_6$PS$_5$Cl added) and of the HSEs, EIS measurements were performed. Figure 2c,d demonstrates that the conductivity of a mixture of a LiTFSI–PEO solid
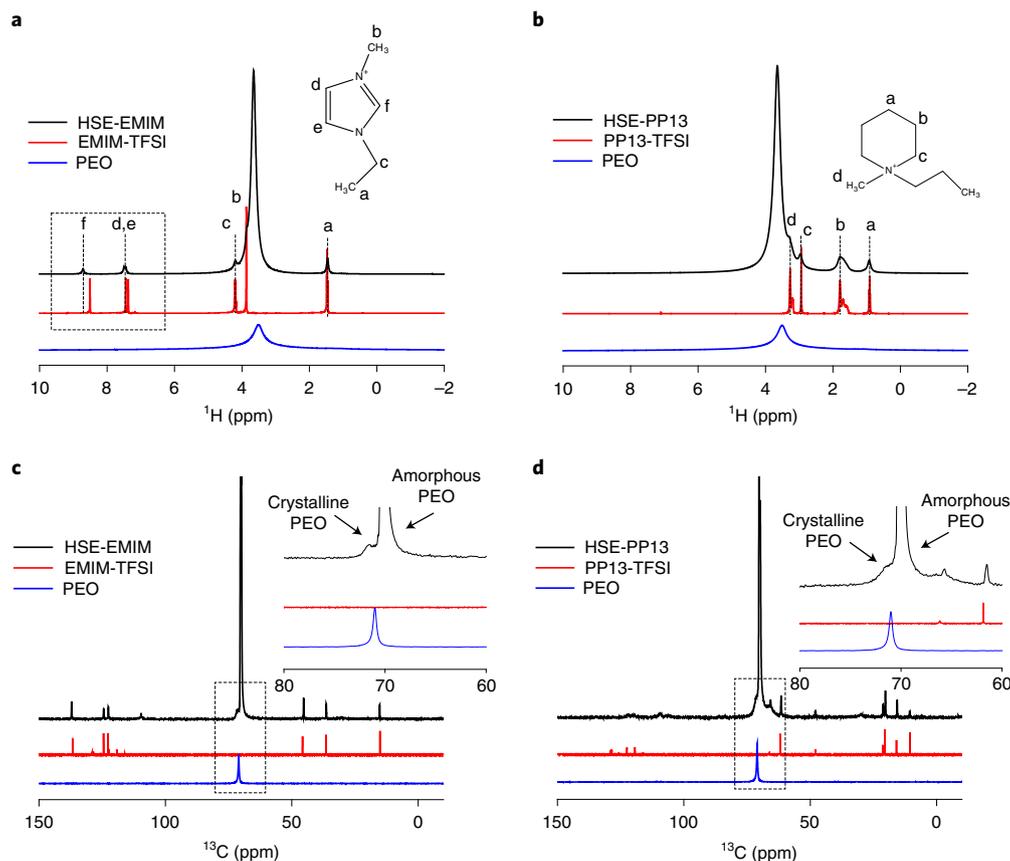
Fig. 3 | Structural characterization of the HSEs with PP13-TFSI and EMIM-TFSI IL additives. a,b, 1D ^{1}H spectra of LiTFSI–PEO–Li_6PS_5Cl HSEs with EMIM-TFSI (HSE-EMIM) and PP13-TFSI (HSE-PP13) ILs. ^{1}H spectra of PEO (solid), EMIM-TFSI (liquid) and PP13-TFSI (liquid) are included for comparison. **c,d**, ^{13}C CPMAS spectra of LiTFSI–PEO–Li_6PS_5Cl HSEs with EMIM-TFSI (HSE-EMIM) and PP13-TFSI (HSE-PP13) ILs. ^{13}C spectra of PEO (solid, CPMAS), EMIM-TFSI (liquid) and PP13-TFSI (liquid) are included for comparison.

polymer electrolyte (SPE) with EMIM-TFSI (SPE-EMIM) is higher than that of the mixture with PP13-TFSI (SPE-PP13), as expected due to the high miscibility of EMIM-TFSI with PEO and in good agreement with previous literature[34]. However, when Li_6PS_5Cl is introduced into the system, the opposite result is found. HSE-PP13 displays a higher conductivity compared to HSE-EMIM and we should also note that both the HSEs have a higher conductivity than the materials without Li_6PS_5Cl. Additionally, the activation energy indicates better conductivity for the HSE-PP13 electrolyte, where the various temperature measurements shown in Fig. 2e give a lower activation energy for HSE-PP13. Clearly, introduction of the inorganic Li_6PS_5Cl in the PEO matrix improved the overall conductivity, indicating that the Li_6PS_5Cl actively contributes to the conductivity[10]. Notably, the poorly miscible PP13-TFSI IL results in a higher conductivity of the HSE as compared to the more miscible EMIM-TFSI IL. This improves the PEO conductivity.

Impact of the ionic liquid on the bulk PEO and PEO–Li_6PS_5Cl interphase structure

To understand the improved conductivity of the HSE upon addition of the poorly miscible PP13-TFSI IL, the structure and kinetics of the PEO–Li_6PS_5Cl interface, which appears to play a critical role in activating the high conductivity of the Li_6PS_5Cl phase, were investigated. The impact of adding the ILs to the bulk PEO structure was investigated first by comparing the ^{1}H and ^{13}C NMR spectra of the individual components. As shown in Fig. 3a, the ^{1}H resonances of EMIM in HSE-EMIM for the peak positions between 6 to 10 ppm show a clear shift compared to pristine EMIM-TFSI, indicating a

change in the ^{1}H environments on the imidazole ring[36]. No change is observed for PP13 (Fig. 3b), reflecting the better miscibility of EMIM-TFSI in PEO. The chemical shifts in the ^{13}C CPMAS spectra (Fig. 3c,d) indicate less crystalline PEO in HSE-EMIM (70 ppm) compared to HSE-PP13 (72 ppm). This is consistent with the better miscibility of EMIM-TFSI in PEO (ref. [37]) and this is further confirmed by the larger decrease in melting temperature when EMIM-TFSI was added (Supplementary Text 1 and Extended Data Fig. 4).

To understand the role of the IL in activating the LiTFSI–PEO–Li_6PS_5Cl interface, the interphase structure was explored using 2D ^{1}H–^{1}H nuclear Overhauser effect spectroscopy (NOESY) NMR measurements (Fig. 4a–f). NOESY is a commonly used method to elucidate polymer structures and configurations[38]. The cross-peaks that arise, especially for short mixing times, are typically between protons that are in close spatial proximity (<1 nm) to each other. As seen from Fig. 4a–c, all the cross-peaks between EMIM-TFSI and LiTFSI–PEO appear at nearly the same mixing time (Extended Data Fig. 5), indicating that there is no preferred orientation of the EMIM-TFSI species with respect to PEO, confirming the good miscibility and that the EMIM-TFSI is mobile. Interestingly, for HSE-PP13 the ^{1}H–^{1}H correlations are first observed (short mixing times) between ^{1}H resonances at positions a and b on the piperidine ring of PP13-TFSI and the –OCH_2– protons from PEO (Fig. 4d–f). This is especially clear from the intensity buildup shown in Extended Data Fig. 5. These ring protons are the furthest away from the bulky propyl and methyl groups attached to the N atom on the piperidine ring. This indicates that the positively charged N
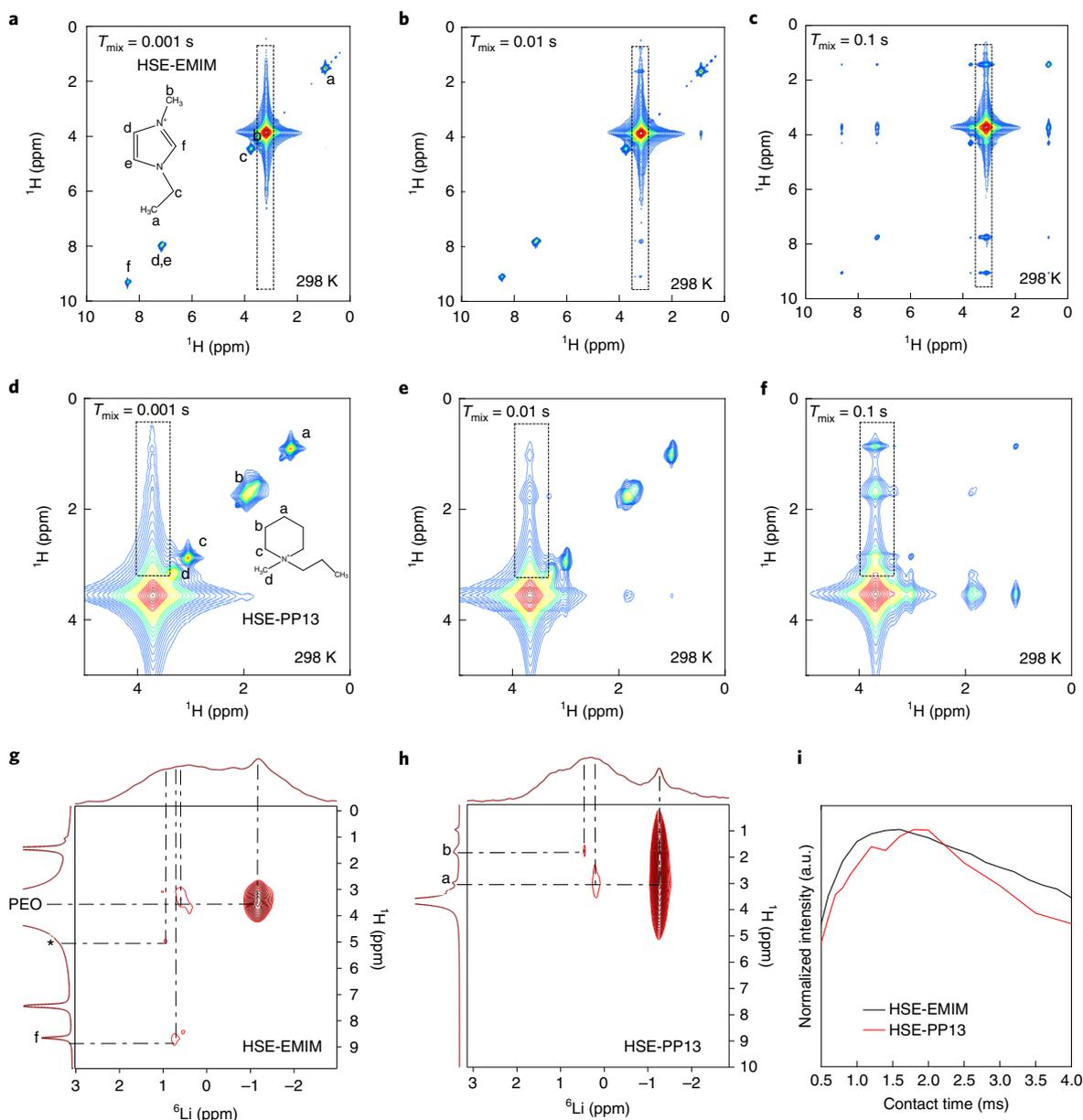
Fig. 4 | Locating the positions of PP13-TFSI and EMIM-TFSI IL additives in the HSEs. a–f, 2D ^1H–^1H NOESY spectra of the mixtures of LiTFSI–PEO–Li$_6$PS$_5$Cl with EMIM-TFSI (**a–c**) and PP13-TFSI (**d–f**) ILs measured at a spinning speed of 5 kHz at 298 K with T_{mix} of 0.001, 0.01 and 0.1 s. The dotted regions indicate the evolution of a series of cross-peaks as a function of T_{mix}. **g,h,** 2D ^1H–^6Li HETCOR spectra of HSE-EMIM and HSE-PP13. **i,** Integrated intensities, denoted in arbitrary units (a.u.), taken from 1D ^7Li CPMAS spectra measured for HSE-EMIM and HSE-PP13 (representative spectra given in Extended Data Fig. 6) at contact times from 200 μs to 4 ms for the Li-interface environment (located at ~0.26 ppm). Intensity from low to high is depicted from blue to red in **a–f**.

atom on the piperidine ring and the functional groups it carries are oriented away from the PEO segments.

Next, the interface environments in both HSEs were explored using 2D ^1H–^6Li HETCOR measurements (Fig. 4g,h). This technique makes it possible to establish which Li-containing species are in proximity to the protons present in PEO and the ILs. For HSE-EMIM (Fig. 4g) a strong correlation is found between PEO and LiTFSI, consistent with the solvation of EMIM in the PEO matrix. Additionally, PEO and EMIM (Fig. 2a) correlate with the decomposed Li$_6$PS$_5$Cl surface species (observed for the HSE without IL, Fig. 1d), indicating that a fraction of the PEO+EMIM is in contact with the Li$_6$PS$_5$Cl particles. For HSE-PP13 (Fig. 4h), no correlations between PEO and LiTFSI or the decomposed Li$_6$PS$_5$Cl species are observed, the former consistent with poor solvation

of this IL in PEO. However, correlations between the protons on the piperidine ring (Fig. 2b) and LiTFSI as well as between the same protons of PP13 with the decomposed Li$_6$PS$_5$Cl surface environments are observed, indicating that PP13 is in contact with Li$_6$PS$_5$Cl. Finally, the PEO–Li$_6$PS$_5$Cl interface was further probed using ^1H–^7Li CPMAS experiments (Fig. 4i), indicating the proximity of protons near the Li$_6$PS$_5$Cl interface for both HSE-PP13 and HSE-EMIM but that there is a difference in proton kinetics between the two interfaces (Supplementary Text 2, Extended Data Fig. 6 and Supplementary Table 1).

To summarize, addition of EMIM-TFSI and PP13-TFSI results in very different PEO bulk and interphase structures in the HSE. ^1H and ^{13}C NMR, as well as differential scanning calorimetry (DSC) measurements, demonstrate that EMIM resides dominantly within
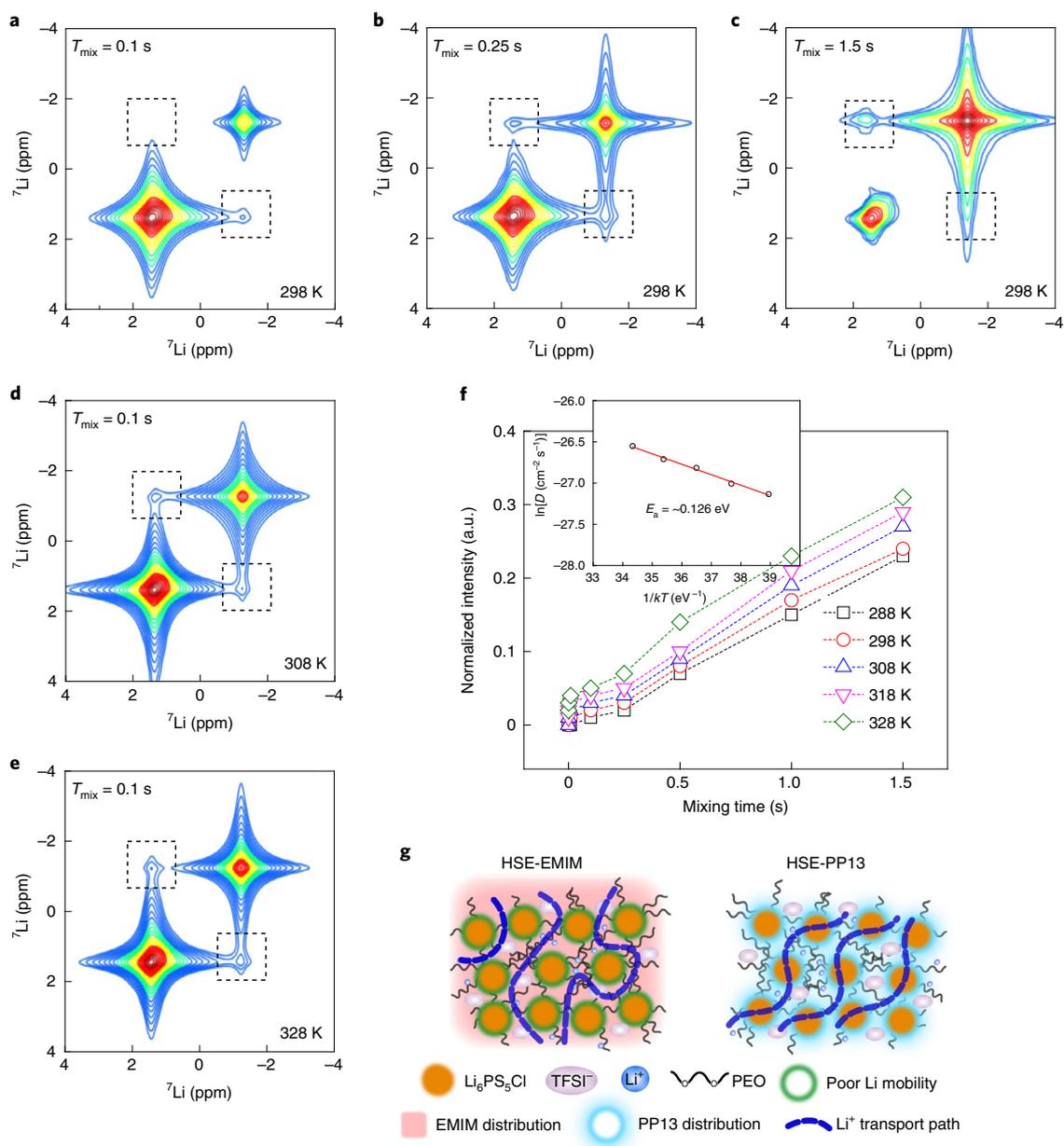
Fig. 5 | Quantification of Li-ion diffusion across phase boundaries in the HSE with the PP13-TFSI IL. a–e, 2D ^{7}Li–^{7}Li EXSY spectra of the mixture of LiTFSI–PEO–Li$_6$PS$_5$Cl with PP13-TFSI IL measured at a spinning speed of 5 kHz at 298 K with mixing times T_{mix} of 0.1, 0.25 and 1.5 s (**a–c**) and at 308 (**d**) and 328 K (**e**) with a T_{mix} of 0.1 s. **f**, Evolution of cross-peak intensity as a function of T_{mix} obtained from the 2D-EXSY measurements performed at the temperatures indicated in the graph. The line passing through the symbols is a guide to the eye. The inset figure is the dependence of the diffusion coefficient (D) obtained from fitting the data in **f** to a diffusion model described by us in detail elsewhere[30]. The normalized intensity is denoted in arbitrary units (a.u.). These can be fitted with the Arrhenius law, yielding an activation energy (E_a) of 0.126 eV. **g**, Proposed mechanism for Li-ion diffusion in HSEs with EMIM-TFSI and PP13-TFSI IL additives. Intensity from low to high is shown from blue to red in **a–e**.

the PEO, thereby lowering the PEO crystalline fraction. The ^{1}H–^{1}H NOESY spectra provide more detail, showing that EMIM has no preferred orientation towards PEO, whereas PP13 does. 2D ^{1}H–^{6}Li HETCOR spectra demonstrate that PP13 is at the surface of the Li$_6$PS$_5$Cl, which in combination with the poor miscibility of PP13 in PEO established above, indicates that PP13 is predominantly located at the PEO–Li$_6$PS$_5$Cl interface, as initially hypothesized.

Impact of the ionic liquid on the interfacial diffusion between LiTFSI–PEO and Li$_6$PS$_5$Cl

To understand how the Li-ion diffusion (due to equilibrium charge transfer) over the PEO–Li$_6$PS$_5$Cl interface of the HSE is affected

by both ILs, ^{6,7}Li–^{6,7}Li 2D-EXSY NMR measurements were conducted, remembering that for the HSE without IL no Li-ion diffusion could be detected (Fig. 1b,c). For HSE-EMIM (Extended Data Fig. 7a,b), no cross-peaks are observed with mixing times as long as 2 s, indicating that there is no significant Li-ion diffusion over the LiTFSI–PEO–Li$_6$PS$_5$Cl interface at this timescale. By contrast, clear cross-peaks, corresponding to Li-ion diffusion between the LiTFSI–PEO and Li$_6$PS$_5$Cl phases, appear for HSE-PP13 (Fig. 5 and Extended Data Fig. 7c,d). This indicates more facile diffusion over the organic–inorganic interface in the HSE-PP13, which is associated with the presence of the PP13 at the PEO–Li$_6$PS$_5$Cl interface established in the previous section.
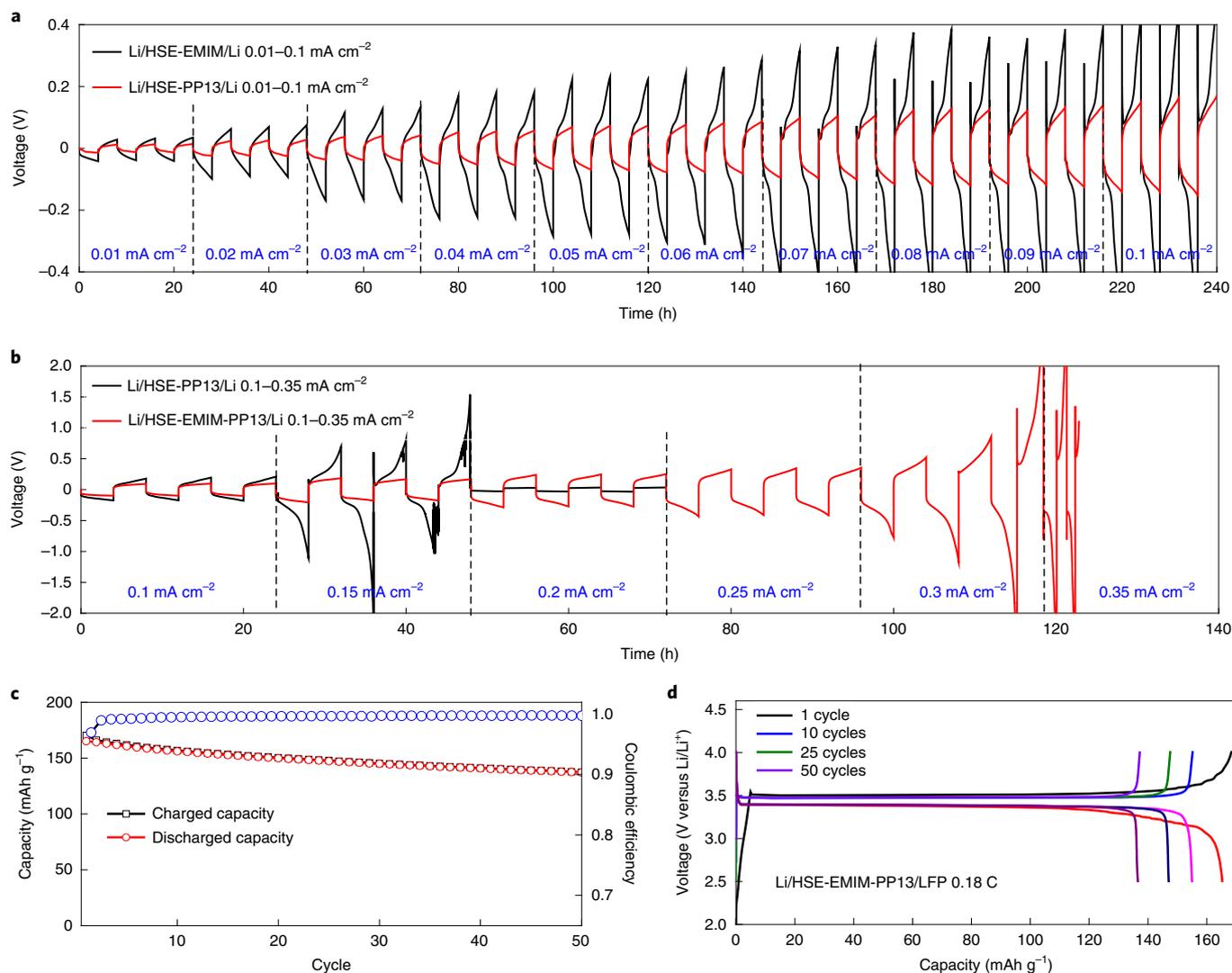
Fig. 6 | Electrochemical characterization of the HSE with PP13-TFSI and EMIM-TFSI IL additives. a, Plating and stripping curves of a Li-metal symmetrical cell (Li/HSE/Li) with LiTFSI–PEO–Li_6PS_5Cl HSEs containing PP13-TFSI (HSE-PP13) or EMIM-TFSI (HSE-EMIM) ILs measured at room temperature. **b**, Plating and stripping curves of a symmetrical cell with LiTFSI–PEO–Li_6PS_5Cl HSE only with PP13-TFSI and with a mixture of PP13-TFSI and EMIM-TFSI (PP13-TFSI and EMIM-TFSI, 0.25:1 molar ratio IL:Li-ion, HSE-PP13-EMIM) ILs measured at room temperature. **c,d**, Specific charge/discharge capacity (red circles) and Coulombic efficiency (blue circles) as a function of cycle number (**c**) and charge and discharge voltage curves (**d**) for a $LiFePO_4$(LFP)/HSE-EMIM-PP13/Li battery cycled at 0.18 C and at room temperature. The red, pink, navy and magenta curves in **d** represent the discharge curves for 1, 10, 25 and 50 cycles.

Upon increasing the mixing time and the temperature, a clear increase in cross-peak intensity is observed (Fig. 5a–e). The Li-ion exchange between the LiTFSI–PEO and Li_6PS_5Cl phases was quantified by fitting the evolution of the cross-peak intensity as a function of T_{mix} (Supplementary Text 3 and Fig. 5f) to a diffusion model derived from Fick's law, described elsewere[29,30,39]. The diffusion coefficient as a function of temperature obtained from the fit (inset Fig. 5f), reflects the Li-ion self-diffusion across the LiTFSI–PEO–Li_6PS_5Cl interface. Fitting with an Arrhenius law yields an activation energy of 0.126 eV for diffusion between the organic and inorganic components, significantly lower than that reported with impedance measurements[26,27]. This suggests that addition of the PP13-TFSI IL 'activates' the LiTFSI–PEO–Li_6PS_5Cl interface, even though micron-sized inorganic argyrodite filler particles are used in the HSE. Thus, there is a relatively small ionic contact area.

Based on these observations, we can now link the PEO–Li_6PS_5Cl interface nanostructure with the Li-ion mobility over the interface.

The poor Li-ion diffusivity over the interface between PEO and Li_6PS_5Cl in the HSE can be rationalized by the observed $-OCH_2-$ groups at the interface (Fig. 1) that annihilate the conducting ethereal oxygen positions that mediate the Li-ion conductivity in PEO. The consequence is that Li-ion transport will be forced though the polymer phase and will not utilize the high conductivity of the Li_6PS_5Cl phase (Fig. 1f). In contrast to the miscible EMIM-TFSI, which improves the conductivity of the PEO, the much less miscible PP13-TFSI settles at the interface with the Li_6PS_5Cl phase (Fig. 5g) where it leads to a higher local mobility. This is held responsible for the facile Li-ion diffusivity over the PEO–Li_6PS_5Cl interface as quantified by the 2D-EXSY experiments in Fig. 5 and can be explained by the higher local mobility induced by the PP13-TFSI IL. The higher dielectric constant of the IL ($\varepsilon > 20$) compared to that of PEO ($\varepsilon \sim 5$) may also play a role[40], thus enhancing the local polarizability. Facilitated by the higher Li-ion diffusivity over the inorganic–organic interface in the presence of PP13-TFSI, long-range

Li-ion transport can now make use of the much higher conductivity of the Li_6PS_5Cl phase (Fig. 5g). This explains the higher overall conductivity of the HSE-PP13 electrolyte observed with EIS (Fig. 2c,d).

Electrochemical evaluation of the hybrid solid electrolyte upon introduction of ionic liquids

As Li metal is the ultimate anode from the perspective of battery energy density, the impact of the IL on the interface of the HSE with Li metal was evaluated in Li-metal symmetrical cells for both HSE-PP13 and HSE-EMIM electrolytes (Fig. 6). The overpotential of the symmetrical cell is an indicative parameter of the interface stability and ability to conduct Li ions[25]. In Fig. 6a, the Li/HSE-EMIM/Li cell shows a continuous increase in overpotential when the current density is higher than $0.05\,mA\,cm^{-2}$, indicating insufficient Li-ion conductivity. By contrast, the Li/HSE-PP13/Li cell shows a much more stable overpotential, increasing with current density up to a relatively small value not exceeding $200\,mV$ at $0.1\,mA\,cm^{-2}$. A similar trend is observed upon cycling (Extended Data Fig. 8). Taking it one step further, we can assume that in the HSE-PP13 electrolyte the conductivity is no longer limited by the $PEO–Li_6PS_5Cl$ interface due to the presence of PP13 but by the polymer phase. To evaluate this, an HSE was prepared with both the PP13-TFSI and EMIM-TFSI additives. In this HSE, PP13-TFSI will enhance the interfacial Li-ion diffusivity while EMIM-TFSI is expected to enhance the Li-ion diffusivity in the PEO phase by improving the chain mobility. Indeed, the small fraction of IL mixture increases the ionic conductivity to $2.47 \times 10^{-4}\,S\,cm^{-1}$ at $25\,°C$ as measured by EIS (Extended Data Fig. 9). The higher conductivity upon adding both ILs is accompanied by a higher critical current density of $0.25\,mA\,cm^{-2}$ (Fig. 6b) as compared to addition of the individual IL additives (Fig. 6a). In theory, a critical current density of $0.25\,mA\,cm^{-2}$ could already enable a solid-state battery using Li–S as the cathode having an energy density of more than $500\,Wh\,kg^{-1}$ (ref. [41]). The HSE with both ILs added demonstrates a critical current density that can be compared to those of state-of-the-art solid-state electrolytes reported in the literature (Supplementary Table 2), although it should be realized that our result is achieved using a small fraction of a liquid (IL) phase. Finally, the HSE with the dual IL additives was electrochemically cycled in a Li-metal battery in combination with a $LiFePO_4$ cathode (Fig. 6c,d). The battery delivers a capacity of more than $0.8\,mAh$ ($120\,mAh\,g^{-1}$) after 50 cycles, with an average Coulombic efficiency of ~99.9% and an overpotential of $150\,mV$, indicating the feasibility of this HSE to function as a solid-state electrolyte for a room-temperature Li-metal battery.

Conclusions

In conclusion, we propose that the bottleneck for Li-ion transport in HSEs comprising PEO polymer and inorganic solid electrolyte phases is across the organic–inorganic phase boundaries, where the deficiency of ethereal oxygen species and absence of local mobility are held responsible for the poor local Li-ion conductivity at the interface. The interface diffusivity can be improved by making use of an IL additive as a wetting agent, in this case PP13-TFSI, whose low miscibility in PEO forces it to be positioned at the phase boundaries where it functions as a bridge for Li-ion transport. The multinuclear solid-state NMR investigation revealed the structure of the interface between the organic and inorganic phases in the HSE and how this affects the Li-ion diffusion pathway. This sheds light on the development of interface strategies, such as the one proposed with non-miscible ILs, leading to improved conductivities and compatibility with Li-metal anodes.

Online content

Any methods, additional references, Nature Research reporting summaries, source data, extended data, supplementary information, acknowledgements, peer review information; details of author contributions and competing interests; and statements of data and code availability are available at https://doi.org/10.1038/s41565-022-01162-9.

References

1. Armand, M. & Tarascon, J.-M. Building better batteries. *Nature* **451**, 652–657 (2008).
2. Dunn, B., Kamath, H. & Tarascon, J.-M. Electrical energy storage for the grid: a battery of choices. *Science* **334**, 928–935 (2011).
3. Cheng, X. B., Zhao, C. Z., Yao, Y. X., Liu, H. & Zhang, Q. Recent advances in energy chemistry between solid-state electrolyte and safe lithium-metal anodes. *Chem* **5**, 74–96 (2019).
4. Zaman, W., Hortance, N., Dixit, M. B., De Andrade, V. & Hatzell, K. B. Visualizing percolation and ion transport in hybrid solid electrolytes for Li-metal batteries. *J. Mater. Chem. A* **7**, 23914–23921 (2019).
5. Armand, M. The history of polymer electrolytes. *Solid State Ion.* **69**, 309–319 (1994).
6. Bouchet, R. et al. Single-ion BAB triblock copolymers as highly efficient electrolytes for lithium-metal batteries. *Nat. Mater.* **12**, 452–457 (2013).
7. Ma, Q. et al. Single lithium-ion conducting polymer electrolytes based on a super-delocalized polyanion. *Angew. Chem. Int. Ed.* **55**, 2521–2525 (2016).
8. Dixit, M. B. et al. Scalable manufacturing of hybrid solid electrolytes with interface control. *ACS Appl. Mater. Interfaces* **11**, 45087–45097 (2019).
9. Osada, I., de Vries, H., Scrosati, B. & Passerini, S. Ionic-liquid-based polymer electrolytes for battery applications. *Angew. Chem. Int. Ed.* **55**, 500–513 (2016).
10. Liu, M. et al. Tandem interface and bulk Li-ion transport in a hybrid solid electrolyte with microsized active filler. *ACS Energy Lett.* **4**, 2336–2342 (2019).
11. Yang, K. et al. Stable interface chemistry and multiple ion transport of composite electrolyte contribute to ultra-long cycling solid-state $LiNi_{0.8}Co_{0.1}Mn_{0.1}O_2$/lithium metal batteries. *Angew. Chem. Int. Ed.* **60**, 24668–24675 (2021).
12. Croce, F., Sacchetti, S. & Scrosati, B. Advanced lithium batteries based on high-performance composite polymer electrolytes. *J. Power Sources* **162**, 685–689 (2006).
13. Syzdek, J. et al. Ceramic-in-polymer versus polymer-in-ceramic polymeric electrolytes—A novel approach. *J. Power Sources* **194**, 66–72 (2009).
14. Hassoun, J. & Scrosati, B. A high-performance polymer tin sulfur lithium ion battery. *Angew. Chem. Int. Ed.* **49**, 2371–2374 (2010).
15. Płcharski, J. & Weiczorek, W. PEO based composite solid electrolyte containing nasicon. *Solid State Ion.* **28**, 979–982 (1988).
16. Xu, K. Electrolytes and interphases in Li-ion batteries and beyond. *Chem. Rev.* **114**, 11503–11618 (2014).
17. Lei, D. et al. Cross-linked beta alumina nanowires with compact gel polymer electrolyte coating for ultra-stable sodium metal battery. *Nat. Commun.* **10**, 4244 (2019).
18. Zheng, J., Tang, M. X. & Hu, Y. Y. Lithium ion pathway within $Li_7La_3Zr_2O_{12}$-polyethylene oxide composite electrolytes. *Angew. Chem. Int. Ed.* **55**, 12538–12542 (2016).
19. Wang, S. et al. A dendrite-suppressed flexible polymer-in-ceramic electrolyte membrane for advanced lithium batteries. *Electrochim. Acta* **353**, 136604 (2020).
20. Fergus, J. W. Ceramic and polymeric solid electrolytes for lithium-ion batteries. *J. Power Sources* **195**, 4554–4569 (2010).
21. Blanga, R., Burstein, L., Berman, M., Greenbaum, S. & Golodnitsky, D. Solid polymer-in-ceramic electrolyte formed by electrophoretic deposition. *J. Electrochem. Soc.* **162**, D3084–D3089 (2015).
22. Chen, L. et al. PEO/garnet composite electrolytes for solid-state lithium batteries: from "ceramic-in-polymer" to "polymer-in-ceramic". *Nano Energy* **46**, 176–184 (2018).
23. Huo, H. Y. et al. Rational design of hierarchical "ceramic-in-polymer" and "polymer-in-ceramic" electrolytes for dendrite-free solid-state batteries. *Adv. Energy Mater.* **9**, 1804004 (2019).
24. Bonizzoni, S. et al. NASICON-type polymer-in-ceramic composite electrolytes for lithium batteries. *Phys. Chem. Chem. Phys.* **21**, 6142–6149 (2019).
25. Dixit, M. B. et al. Nanoscale mapping of extrinsic interfaces in hybrid solid electrolytes. *Joule* **4**, 207–221 (2020).
26. Simon, F. J. et al. Properties of the interphase formed between argyrodite-type Li_6PS_5Cl and polymer-based PEO_{10}:LiTFSI. *ACS Appl. Mater. Interfaces* **11**, 42186–42196 (2019).
27. Simon, F. J., Hanauer, M., Richter, F. H. & Janek, J. Interphase formation of PEO_{20}:LiTFSI–Li_6PS_5Cl composite electrolytes with lithium metal. *ACS Appl. Mater. Interfaces* **12**, 11713–11723 (2020).
28. Zheng, J., Wang, P., Liu, H. & Hu, Y.-Y. Interface-enabled ion conduction in $Li_{10}GeP_2S_{12}$-poly (ethylene oxide) hybrid electrolytes. *ACS Appl. Energy Mater.* **2**, 1452–1459 (2019).

29. Yu, C. et al. Accessing the bottleneck in all-solid state batteries, lithium-ion transport over the solid-electrolyte-electrode interface. *Nat. Commun.* **8**, 1086 (2017).
30. Ganapathy, S., Yu, C., van Eck, E. R. H. & Wagemaker, M. Peeking across grain boundaries in a solid-state ionic conductor. *ACS Energy Lett.* **4**, 1092–1097 (2019).
31. Schwietert, T. K. et al. Clarifying the relationship between redox activity and electrochemical stability in solid electrolytes. *Nat. Mater.* **19**, 428–435 (2020).
32. Hoefling, A. et al. Mechanism for the stable performance of sulfur-copolymer cathode in lithium–sulfur battery studied by solid-state NMR spectroscopy. *Chem. Mater.* **30**, 2915–2923 (2018).
33. Rataboul, F. et al. Molecular understanding of the formation of surface zirconium hydrides upon thermal treatment under hydrogen of [(≡SiO)Zr(CH₂*t*Bu)₃] by using advanced solid-state NMR techniques. *J. Am. Chem. Soc.* **126**, 12541–12550 (2004).
34. Zhu, C., Cheng, H. & Yang, Y. Electrochemical characterization of two types of PEO-based polymer electrolytes with room-temperature ionic liquids. *J. Electrochem. Soc.* **155**, A569 (2008).
35. Kodama, K. et al. Structural effects of polyethers and ionic liquids in their binary mixtures on lower critical solution temperature liquid-liquid phase separation. *Polym. J.* **43**, 242–248 (2011).
36. Cesare Marincola, F. et al. NMR investigation of imidazolium-based ionic liquids and their aqueous mixtures. *ChemPhysChem* **13**, 1339–1346 (2012).
37. Wang, B.-H., Xia, T., Chen, Q. & Yao, Y.-F. Probing the dynamics of Li⁺ ions on the crystal surface: a solid-state NMR study. *Polymers* **12**, 391 (2020).
38. Zhao, Z. et al. Ionic-association-assisted viscoelastic nylon electrolytes enable synchronously coupled interface for solid batteries. *Adv. Funct. Mater.* **30**, 2000347 (2020).
39. Ganapathy, S., van Eck, E. R., Kentgens, A. P., Mulder, F. M. & Wagemaker, M. Equilibrium lithium-ion transport between nanocrystalline lithium-inserted anatase TiO₂ and the electrolyte. *Chem. Eur. J.* **17**, 14811–14816 (2011).
40. Kumar, M. & Sekhon, S. S. Role of plasticizer's dielectric constant on conductivity modification of PEO–NH₄F polymer electrolytes. *Eur. Polym. J.* **38**, 1297–1304 (2002).
41. Liu, M. et al. Novel gel polymer electrolyte for high-performance lithium–sulfur batteries. *Nano Energy* **22**, 278–289 (2016).

Methods

The solid-state electrolyte Li_6PS_5Cl was prepared by a simple solid-state reaction. The stoichiometric raw materials LiCl (Sigma-Aldrich), P_2S_5 (Sigma-Aldrich) and Li_2S (Sigma-Aldrich) were used as the starting materials and were ball-milled at 110 rpm for 2 h with ZrO_2-coated jars using 18 ZrO_2 balls. After the ball milling, the precursor was sealed in a quartz tube containing Ar and then annealed at 550 °C for 15 h to obtain the Li_6PS_5Cl solid electrolyte.

HSE films were prepared by mixing 0.768 g PEO (Sigma-Aldrich, $M_w = 600,000$), 0.28 g LiTFSI (Sigma-Aldrich), 0.1048 g Li_6PS_5Cl and 0.25:1 molar ratio IL:Li-ion ionic liquid together in 10 ml acetonitrile (Sigma-Aldrich) and stirring for 24 h. The prepared solution was evenly casted onto a Teflon plate and dried in the glove box at room temperature for 24 h, then transferred into a reduced pressure environment in the glove box for 48 h. DSC measurements were carried out at 10° min⁻¹ steps using a commercial TA-Q2000 DSC calorimeter (TA instruments). The morphology of HSE was analysed using an SEM (JEOL JSM IT100LA).

Linear-sweep voltammetry (LSV) was performed on a cell of Li/HSE/SS with a stainless steel (SS) area of 1.13 cm². The LSV curves were recorded from the open-circuit voltage (OCV) to 5.5 V versus Li/Li-ion at a scanning rate of 0.1 mV s⁻¹ using an Autolab PGSTAT302N (Metrohm-Autolab). The ionic conductivities of the HSEs were measured using EIS, where the HSE was sandwiched between two SS blocking electrodes (area 1.13 cm²) and kept at each test temperature (from 25 to 85 °C) for at least 30 min, in order to reach thermal equilibrium, before the electrochemical impedance measurements were acquired. The EIS measurements were obtained using an Autolab PGSTAT302N in the frequency range 10 MHz–1 kHz with a sinusoidal signal with $V_{rms} = 10$ mV. EIS spectra were fitted with an equivalent circuit (EC) model, where R_S is the series resistance, R_b is the bulk polymer resistance and CPE_b is a constant phase element (CPE) which accounts for the bulk capacitance of the polymer film and CPE_{int} accounts for the capacitance associated with the blocking electrodes at low frequencies. From this, the bulk resistance (R_b) and the ionic conductivity (σ) are calculated using the equation $\sigma = d/(R_b \times A)$, where d is the thickness and A is the area of polymer electrolyte in contact with the SS (1.13 cm² in our case). The HSE-based all-solid-state cells were assembled in an Ar-filled glove box. These cells consisted of lithium metal (Aldrich) and $LiFePO_4$ (denoted as LFP, mass loading: ~6.5 mg cm⁻²) as electrodes and the HSE as the electrolyte. It should be noted that 50 μl of the HSE solution prepared with the above methods was dropped into an LFP electrode and then allowed to dry fully. $LiFePO_4$ (Sigma-Aldrich) cathodes were prepared by mixing the active material with Super P and polyvinylidene fluoride (PVDF) in a mass ratio of 8:1:1 and N-Methylpyrrolidone (NMP) was used as a solvent. Charge–discharge tests of the HSE-based all-solid-state cells were performed using a Maccor 4000 battery cycler at room temperature.

Solid-state NMR measurements were performed using a Bruker Ascend 500 magnet ($B_0 = 11.7$ T) with an NEO console operating at frequencies of 500.130 MHz for ¹H, 194.37 MHz for ⁷Li, 73.6 MHz for ⁶Li and 125.758 MHz for ¹³C. ⁶,⁷Li chemical shifts were referenced with respect to a 0.1 M LiCl solution (0 ppm) and ¹H and ¹³C chemical shifts were referenced with respect to solid adamantane (¹H at 1.81 ppm and ¹³C at 38.48 ppm). A Bruker three-channel MAS 4 mm direct variable temperature (DVT) probe was used for all measurements. The LiTFSI–PEO–Li_6PS_5Cl (HSE), HSE-EMIM and HSE-PP13 membranes were cut into tiny pieces and filled into 4 mm zirconia rotors that were spun at speeds of 5 kHz for all measurements. One-pulse ¹H, ⁷Li and ⁶Li experiments were performed with π/2 pulse lengths of 3.5, 2.7 and 4.75 μs respectively. A recycle delay of three times T_1 was used each time, where T_1 was determined using saturation recovery experiments. 2D ⁷Li–⁷Li and ⁶Li–⁶Li EXSY measurements were performed for these samples at various mixing times from 1 ms up to 2 s and at temperatures from 10 to 50 °C. Each spectrum consisted of 8 (16) scans for each of the 1,200–1,500 (400–800) transients, each transient incremented by 200 (400) μs with a recycle delay of up to 5 (10) s. The ⁶Li CPMAS experiments were performed with an initial ¹H π/2 pulse of 5 μs. During CP, for ⁶Li, radio frequency (r.f.) field strengths of 25 kHz and contact times of up to 6 ms were utilized. The r.f. field amplitude of

¹H during CP was ramped from 70 to 100% and 256 (1,024) scans were acquired for each sample with a recycle delay of 2 (3) s. 2D ¹H–⁶Li HETCOR measurements were performed with a short CP contact time of 0.2 ms for the HSE and long contact times of 10 ms each for the HSE-EMIM and HSE-PP13. For each of the 128 transients in the indirect ¹H dimension, 128 ⁶Li scans were accumulated. A recycle delay of 3 s was applied after each scan. The ¹³C CPMAS experiments were measured with an initial ¹H π/2 pulse of 3.65 μs. During CP for ¹³C, an r.f. field strength of 58 kHz was utilized and 40,000 scans were acquired for each sample with a recycle delay of 2 s. For both the CPMAS and HETCOR experiments, proton decoupling was performed during acquisition using the SPINAL-64 decoupling sequence[42]. 2D ¹H–¹H NOESY measurements were performed at various mixing times from 1 ms to 100 ms at room temperature. Each spectrum consisted of 8 scans for each of the 800 transients, with each transient incremented by 100 μs with a recycle delay of 2 s. ⁷Li CPMAS experiments were performed on an Agilent 400 MHz spectrometer operating at 155.422 MHz for ⁷Li and 399.915 MHz for ¹H. A 4 mm HXY Chemagnetics pencil design probe was used at an MAS speed of 5 kHz. For CP both the ¹H and ⁷Li r.f. field strengths were set at 40 kHz and SPINAL-64 proton decoupling at the same field strength with 12.5 μs pulse length and an 8° phase shift was used during acquisition.

Data availability

The data that support the findings of this study are available at the online depository Zenodo (https://doi.org/10.5281/zenodo.6334099).

References

42. Fung, B., Khitrin, A. & Ermolaev, K. An improved broadband decoupling sequence for liquid crystals and solids. *J. Magn. Reson.* **142**, 97–101 (2000).

Author contributions

S.G. and M.W. designed and supervised the research. M.L., S.Z. and C.W. synthesized and characterized the hybrid solid electrolytes. M.L. and S.Z. carried out the electrochemical measurements. M.L., S.G. and E.R.H.v.E. measured and analysed the NMR data. M.L., S.G. and M.W. wrote the manuscript.

Competing interests

The authors declare no competing interests.

Additional information

Extended data is available for this paper at https://doi.org/10.1038/s41565-022-01162-9.

Supplementary information The online version contains supplementary material available at https://doi.org/10.1038/s41565-022-01162-9.

Correspondence and requests for materials should be addressed to Swapna Ganapathy or Marnix Wagemaker.

Peer review information *Nature Nanotechnology* thanks Ye-Feng Yao and the other, anonymous, reviewer(s) for their contribution to the peer review of this work.

**Reprints and permissions information** is available at www.nature.com/reprints.
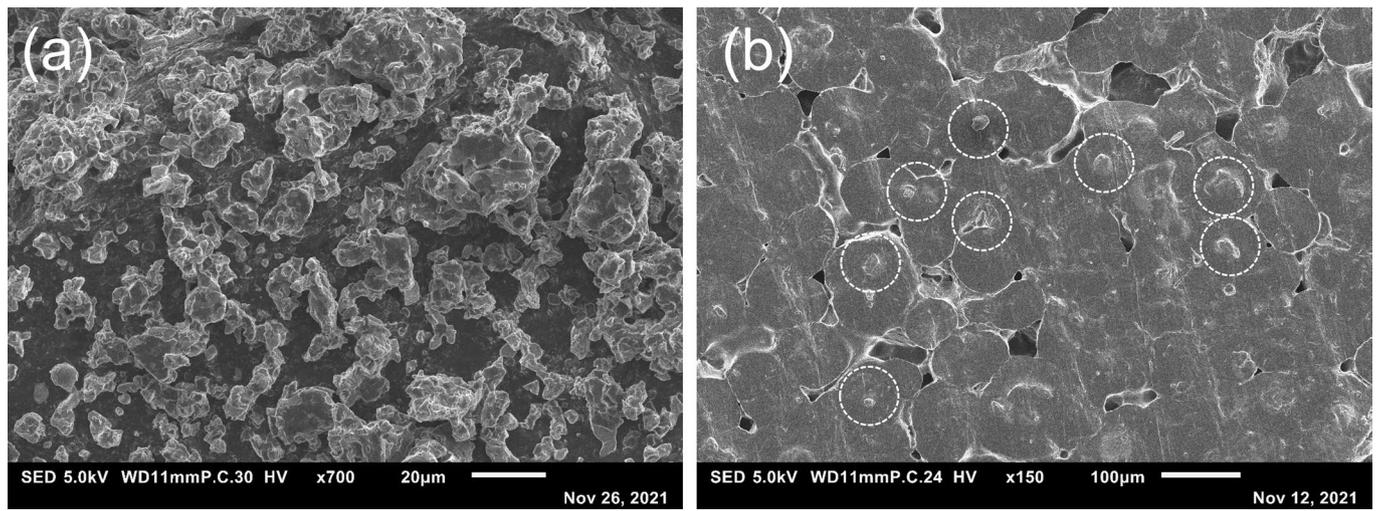
Extended Data Fig. 1 | SEM image of the pristine micron-sized Li$_6$PS$_5$Cl and LiTFSI-PEO-Li$_6$PS$_5$Cl HSE. (**a**) SEM image of the pristine micron-sized Li$_6$PS$_5$Cl. (**b**) SEM image showing the morphology of the HSE where the Li$_6$PS$_5$Cl particles are marked with circles.
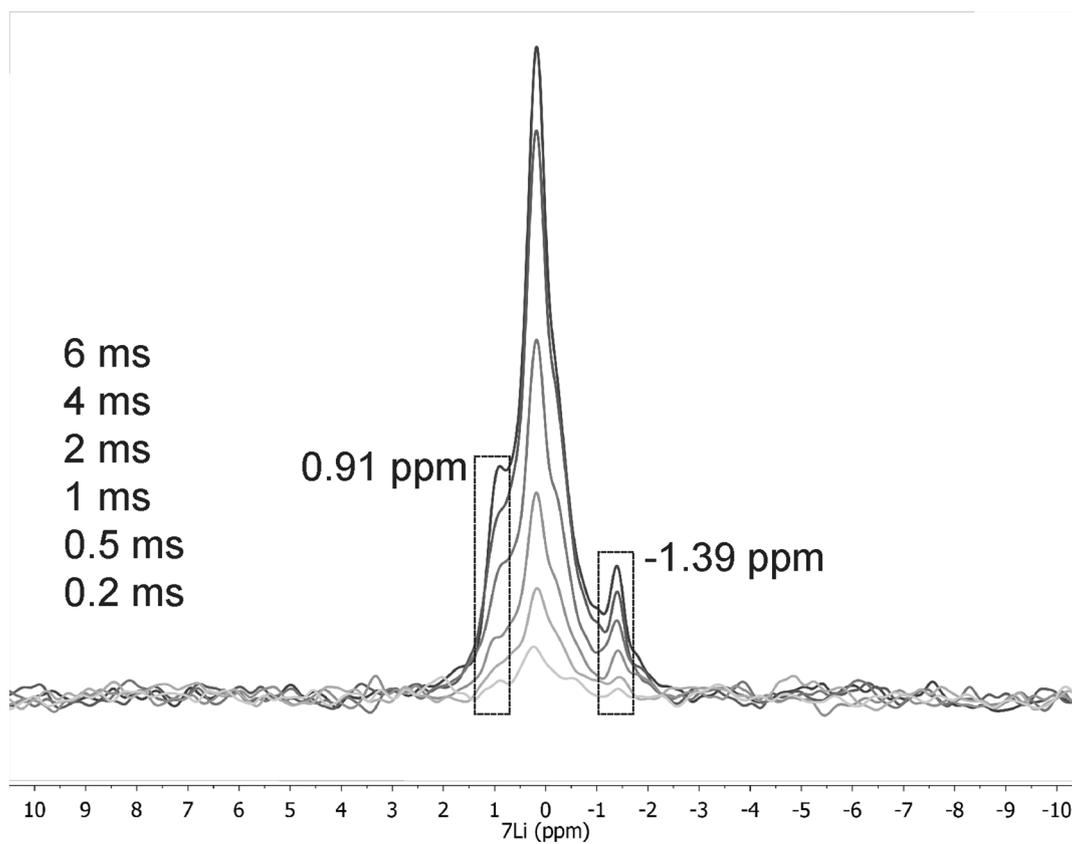
Extended Data Fig. 2 | ^{1}H-^{6}Li CPMAS spectra of the LiTFSI-PEO-Li$_6$PS$_5$Cl HSE. ^{1}H-^{6}Li CPMAS spectra of the LiTFSI-PEO-Li$_6$PS$_5$Cl HSE measured at contact times ranging from 0.2 ms (lightest grey) to 6 ms (black).
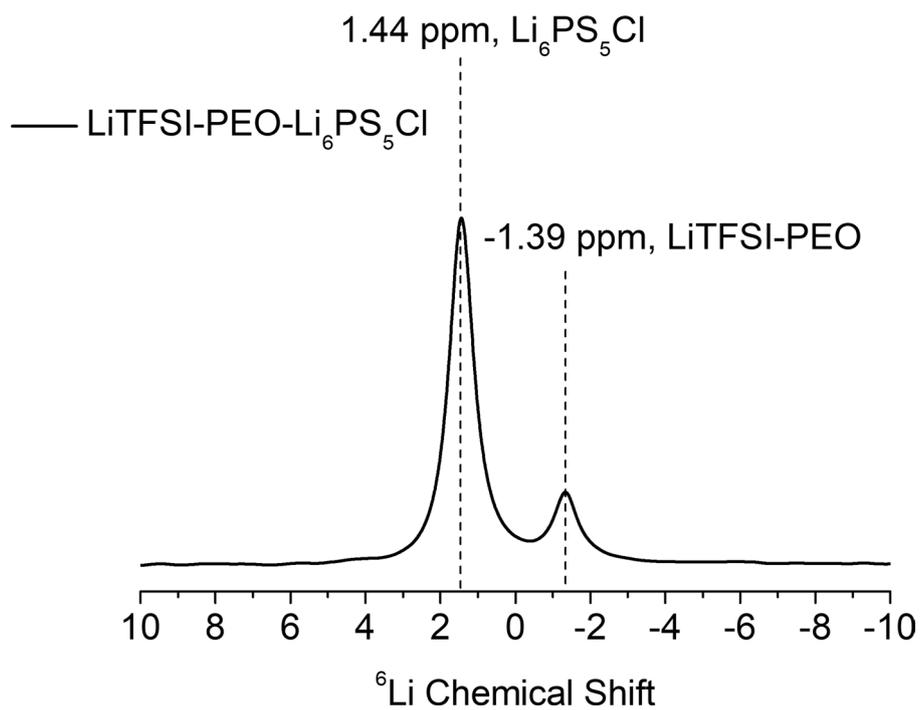
Extended Data Fig. 3 | 1D ^{6}Li magic angle spinning (MAS) spectrum corresponding to the Li$_6$PS$_5$Cl -LiTFSI-PEO HSE. 1D ^{6}Li magic angle spinning (MAS) spectrum corresponding to the Li$_6$PS$_5$Cl -LiTFSI-PEO HSE.
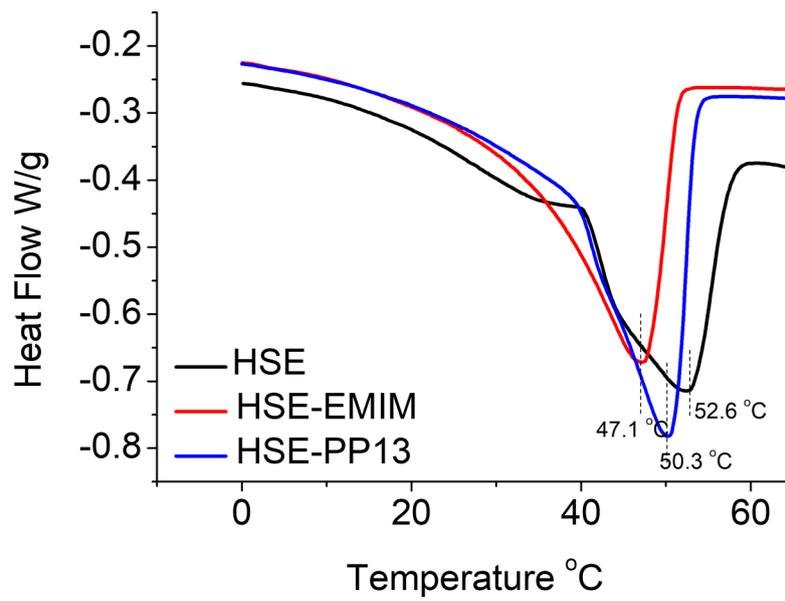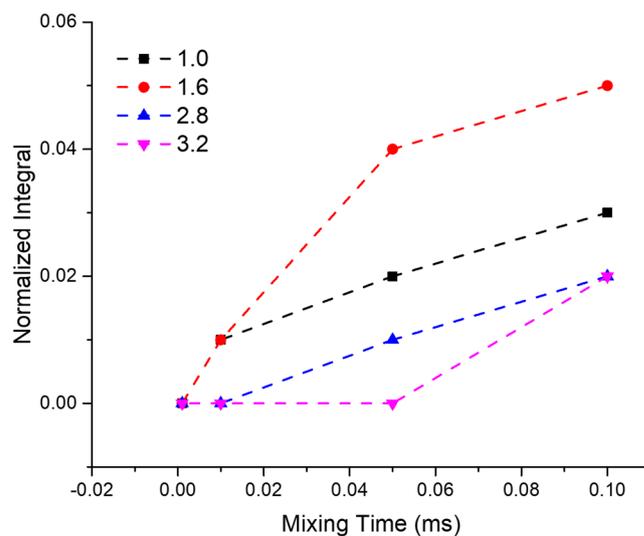
Extended Data Fig. 4 | DSC measurements showing the heat flow of the HSE, HSE-EMIM, HSE-PP13. DSC measurements showing the heat flow of the HSE, HSE-EMIM, HSE-PP13 under heating up from 0 to 65 °C.
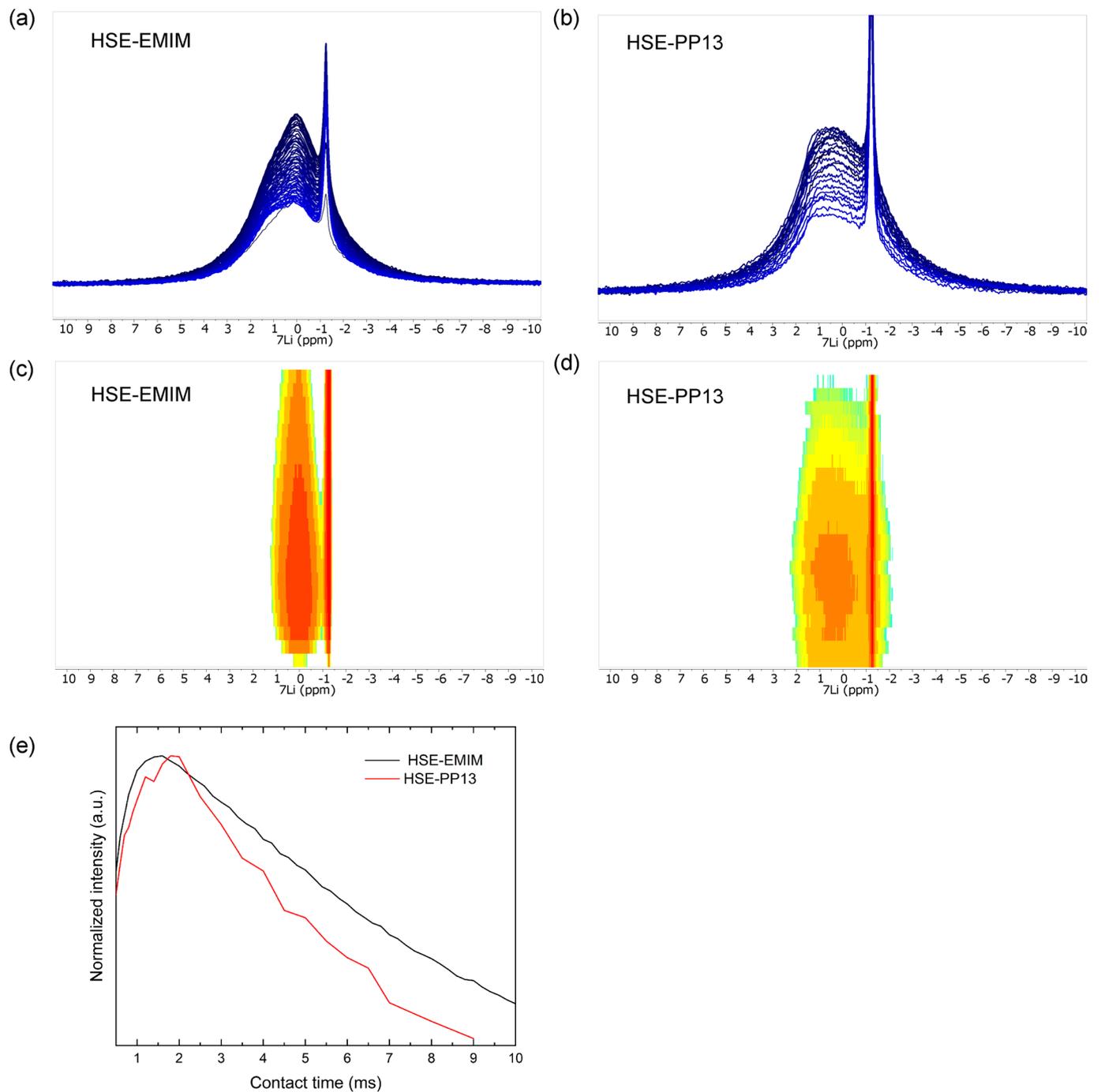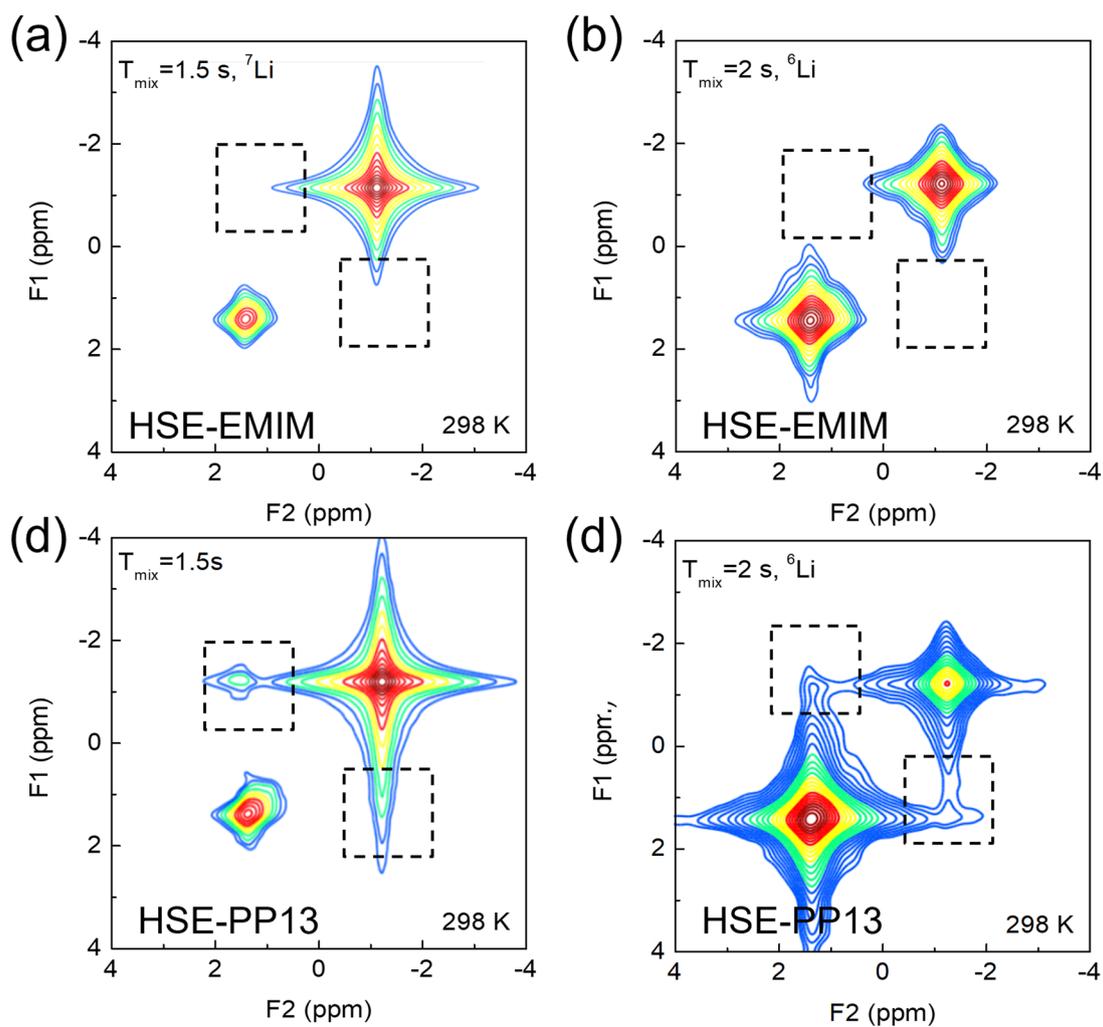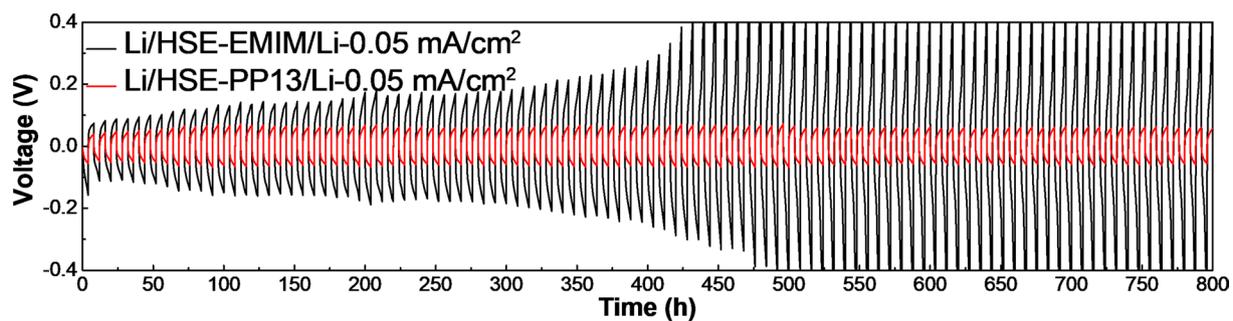
(a) HSE-EMIM
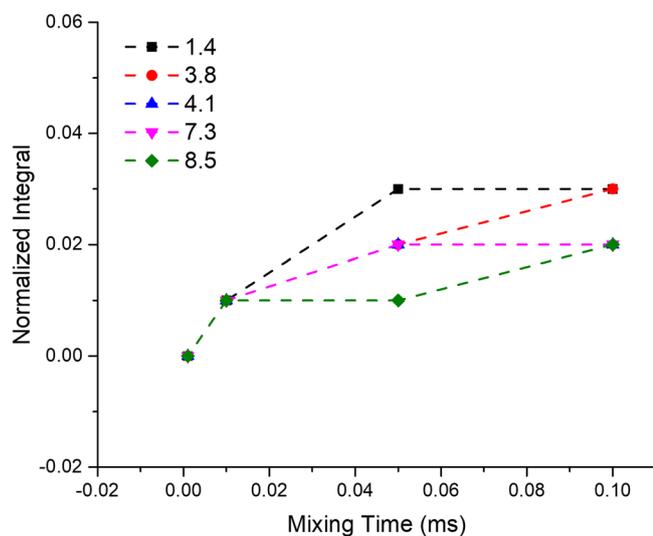
(b) HSE-PP13

Extended Data Fig. 5 | ^{1}H-^{1}H cross peak intensity buildup of protons in EMIM-TFSI and PP13-TFSI correlated to PEO from the 2D ^{1}H-^{1}H NOESY spectra of HSE-PP13 and HSE-EMIM. ^{1}H-^{1}H cross peak intensity buildup of protons in EMIM-TFSI (a) and PP13-TFSI (b) correlated to PEO from the 2D ^{1}H-^{1}H NOESY spectra of HSE-PP13 and HSE-EMIM given in Fig. 4. All the cross peaks between EMIM-TFSI and LiTFSI-PEO appear at nearly at the same mixing time which means that there is no preferred orientation of the EMIM-TFSI species with respect to PEO. While a sequence of cross peak evolution with mixing time is observed in HSE-PP13. At the shortest mixing times, ^{1}H-^{1}H correlations are first observed between ^{1}H resonances at positions 1.0 ppm and 1.6 ppm on the piperidine ring of PP13-TFSI and the –OCH$_2$- protons from PEO. These ring protons are the furthest away from the bulky propyl and methyl groups attached to the N atom on the piperidine ring.

Extended Data Fig. 6 | 1D ^{7}Li CPMAS spectra and intensity plots measured of the HSE-EMIM and HSE-PP13, and the full build-up of the peak intensity of the broad component. 1D ^{7}Li CPMAS spectra and intensity plots measured of the (**a,c**) HSE-EMIM and (**b,d**) HSE-PP13 at contact times between 200 μs and 12 ms (**e**) Full build-up of peak intensity at 0.2–0.7 ppm as function of contact time of the spectra given in (a) and (b).

Extended Data Fig. 7 | Li⁺ transport characterization in HSE-EMIM and HSE-PP13 using 6,7Li-6,7Li 2D EXSY NMR. Li⁺ transport characterization in HSE with PP13-TFSI and EMIM-TFSI IL additives. ⁷Li–⁷Li, ⁶Li-⁶Li 2D-EXSY corresponding to the HSE-EMIM (**a**, **b**) and HSE-PP13 (**c**, **d**) ILs measured under MAS at a spinning speed of 5 kHz mixing time of 1.5 s and 2 s at 328 K.

Extended Data Fig. 8 | Plating and stripping curves of a Li metal symmetrical cell with HSE-EMIM and HSE-PP13. Plating and stripping curves of a Li metal symmetrical cell with LiTFSI-PEO-Li$_6$PS$_5$Cl HSEs with PP13 TFSI and EMIM TFSI ionic liquids. The cell with HSE-EMIM shows quick polarization after 300 h of cycling at a current density of 0.05 mA/cm^2. In comparison the cell with HSE-PP13 shows a very stable over-potential (lower than 200 mV) during 800 hours of cycling, indicating a higher ionic conductivity and better interfacial stability against Li-metal.
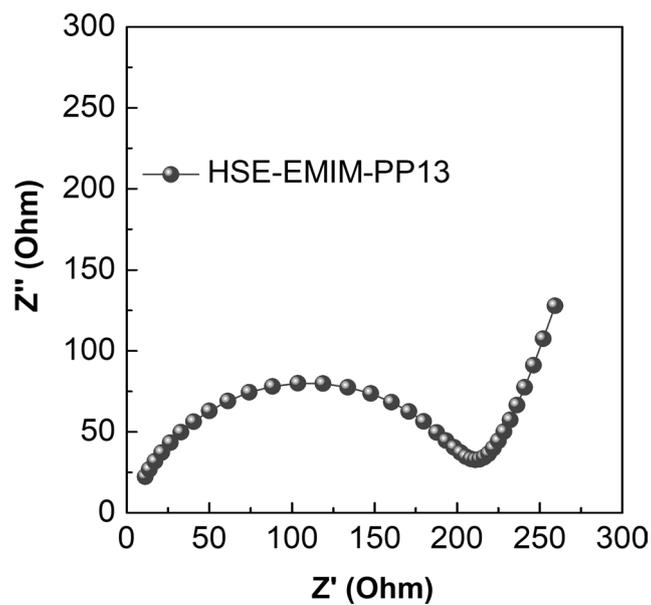
Extended Data Fig. 9 | Electrochemical impedance spectroscopy measurements (EIS) of the cell with LiTFSI-PEO-Li$_6$PS$_5$Cl HSE with both PP13-TFSI and EMIM-TFSI ionic liquids. Electrochemical impedance spectroscopy measurements (EIS) of cell with LiTFSI-PEO-Li$_6$PS$_5$Cl HSE with both PP13-TFSI and EMIM-TFSI (PP13-TFSI and EMIM-TFSI, 0.25:1 molar ratio IL:Li-ion, HSE—EMIM-PP13) ionic liquids.